Anion dynamics in the first 10 milliseconds of an argon–acetylene radio-frequency plasma

Please check the document version of this publication:

• A submitted manuscript is the version of the article upon submission and before peer-review. There can be important differences between the submitted version and the official published version of record. People interested in the research are advised to contact the author for the final version of the publication, or visit the DOI to the publisher's website.
• The final author version and the galley proof are versions of the publication after peer review.
• The final published version features the final layout of the paper including the volume, issue and page numbers.

Link to publication

Download date: 16. Nov. 2023

Anion dynamics in the first 10 milliseconds of an argon–acetylene radio-frequency plasma

Anion dynamics in the first 10 milliseconds of an argon–acetylene radio-frequency plasma

F M J H van de Wetering, J Beckers and G M W Kroesen

Department of Applied Physics, Eindhoven University of Technology, PO Box 513, 5600 MB
Eindhoven, the Netherlands

E-mail: f.m.j.h.v.d.wetering@tue.nl

Abstract
The time evolution of the smallest anions (C_2H^- and H_2CC^-), just after plasma ignition, is studied by means of microwave cavity resonance spectroscopy (MCRS) in concert with laser-induced photodetachment under varying gas pressure and temperature in an argon–acetylene radio-frequency (13.56 MHz) plasma. These anions act as an initiator for spontaneous dust particle formation in these plasmas. With an intense 355 nm Nd : YAG laser pulse directed through the discharge, electrons are detached only from these anions present in the laser path. This results in a sudden increase in the electron density in the plasma, which can accurately and with sub-microsecond time resolution be measured with MCRS. By adjusting the time after plasma ignition at which the laser is fired through the discharge, the time evolution of the anion density can be studied. We have operated in the linear regime: the photodetachment signal is proportional to the laser intensity. This allowed us to study the trends of the photodetachment signal as a function of the operational parameters of the plasma. The density of the smallest anions steadily increases in the first few milliseconds after plasma ignition, after which it reaches a steady state. While keeping the gas density constant, increasing the gas temperature in the range 30–120 °C limits the number of smallest anions and saturates at a temperature of about 90 °C. A reaction pathway is proposed to explain the observed trends.

(Some figures may appear in colour only in the online journal)

1. Introduction

A dusty plasma, or a complex plasma as it is increasingly frequently referred to, is a plasma that—apart from the common neutrals, ions and electrons—also contains nano- to micrometre-sized solid particles. The particles can be either externally introduced into the system or spontaneously formed by the plasma itself. The latter is the subject of this paper. Active dusty plasma research basically started from the early 1990s, both experimentally and theoretically (i.e. models and computer simulations). Plasmas of numerous gases have been found able to—under certain conditions—spontaneously grow dust, e.g. plasmas of silane (SiH_4), methane (CH_4), tetrafluoromethane (CF_4) and acetylene (C_2H_2). Dust particle formation in radio-frequency (RF) silane plasmas was, for example, studied by Stoffels *et al* [1], Sorokin [2] and Boufendi *et al* [3], using microwave cavity resonance spectroscopy (MCRS), where the first two combined it with laser-induced photodetachment (LIP), and the latter two also studied the electrical characteristics of the RF power. Beckers *et al* [4] studied RF methane plasmas using MCRS and laser light scattering. Buss and Hareland [5] studied RF plasmas of fluorocarbons (CF_4, C_2F_4 and 1,1-$C_2H_2F_2$) using laser light scattering and Fourier transform infrared absorption spectroscopy (FTIR). Deschenaux *et al* [6] studied RF plasmas of methane, acetylene and ethylene using FTIR and mass spectrometry. Particle formation in argon–helium–acetylene plasmas was studied by Benedikt *et al* [7] by means of time-resolved mass spectrometry. Stoykov *et al* [8] developed a model for the chemical clustering kinetics in a low-pressure

RF acetylene plasma and compared it with FTIR and nuclear magnetic resonance experiments. De Bleecker *et al* [9] developed a one-dimensional fluid model for the nucleation of hydrocarbon nanoparticles in RF acetylene plasmas. Mao *et al* [10] extended and refined the model by De Bleecker *et al* and compared it with mass spectrometric measurements. Low-pressure argon–acetylene RF plasmas are the type of plasma under investigation here. Particle formation in the same mixture was experimentally studied using laser light scattering in the 'PK-4' facility by Wörner *et al* [11] (dc-driven) and by Mitic *et al* [12] (RF-driven). A pulsed argon–acetylene RF discharge was studied by Berndt *et al* [13].

In RF silane plasmas, dust particle formation is explained using a four-step process [14], which is believed to equally apply to hydrocarbon plasmas [4]. The formation of large molecules (mainly by polymerization) is generally regarded as the first step. Polymerization can be initiated by three types of species: positive ions, negative ions and neutrals. As in RF discharges the walls quickly attain a negative potential (and sheaths form), and the only particles that reside sufficiently long in the plasma bulk to initiate polymerization are negatively charged species. Positive ions and neutral radicals can also polymerize, but the former are accelerated towards the walls whereas the latter diffuse away from the active plasma region. Negative ions are the only species actively trapped in the plasma bulk. During this first step, the clusters predominantly remain singly negatively charged. The formation of negative ions in an acetylene plasma occurs through dissociative electron attachment (DEA) onto acetylene [9],
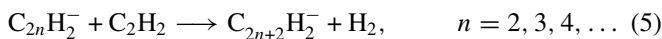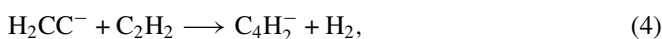
$$C_2H_2 + e^- \longrightarrow C_2H^- + H, \qquad (1)$$
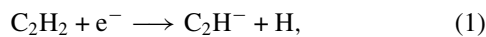
forming the ethynyl anion (C_2H^-), which further polymerizes into larger hydrocarbons,

$$C_{2n}H^- + C_2H_2 \longrightarrow C_{2n+2}H^- + H_2, \qquad n = 1, 2, 3, \ldots, \qquad (2)$$
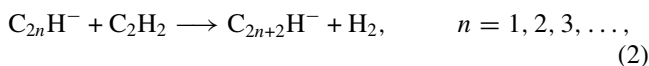
where the initial polymerization of C_2H^- corresponds to $n = 1$. Recently, it was proposed [10] that electron attachment onto acetylene might also yield the vinylidene anion (H_2CC^-),

$$C_2H_2 + e^- \longrightarrow H_2CC^-, \qquad (3)$$

This, then, could also polymerize:

$$H_2CC^- + C_2H_2 \longrightarrow C_4H_2^- + H_2, \qquad (4)$$

$$C_{2n}H_2^- + C_2H_2 \longrightarrow C_{2n+2}H_2^- + H_2, \qquad n = 2, 3, 4, \ldots \quad (5)$$

and initiate dust particle formation. This mechanism was proposed to explain mass spectrometric measurements of Deschenaux *et al* [6].

In the second step, termed nucleation and cluster growth, the clusters grow to a size of several nanometres. There is active charge transfer between the clusters, but most clusters are either singly charged (positive and negative) or neutral. The third step, coagulation, starts when the clusters reach a critical density (for silane this lies between 10^{15} and 10^{18} m^{-3}). Clusters of like charge will not to stick together, but clusters in all the other cases will. This results in particles up to about 50 nm, at which point they act like a plasma probe and become highly and permanently negatively charged. In the final step, the particles may grow to micrometre sizes by deposition of plasma radicals and ions. The particle dynamics and plasma chemistry up to the nucleation phase is the focus of this paper.

2. Experimental method
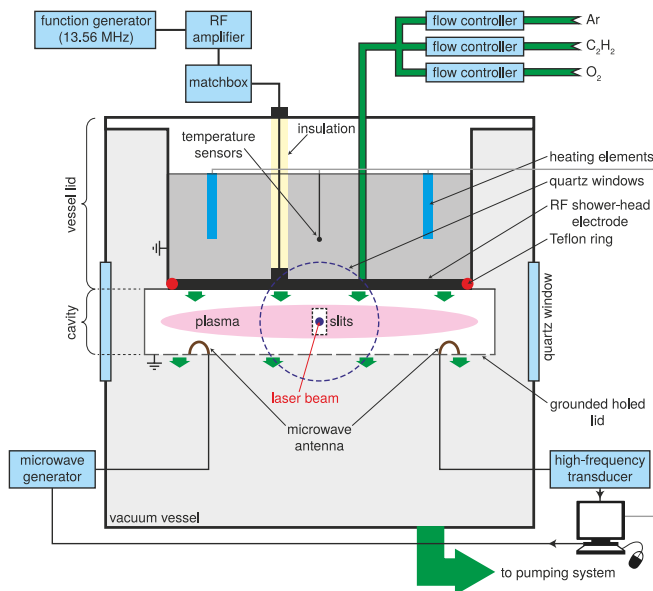
2.1. Experimental setup

The experiments are performed in a grounded stainless steel cylindrical vacuum vessel of 30 cm diameter and 45 cm height. The vessel lid contains a gas inlet connected to a shower-head-shaped electrode. This electrode contains 331 homogeneously distributed holes (0.5 mm in diameter) to ensure homogeneous gas flow below. The vessel lid also contains two PT-100 temperature sensors, four heating elements and a water/air cooling system with which its temperature is controlled within the range 30–120 °C. The electrode simultaneously serves as the powered electrode for RF plasma operation, has a diameter of 138 mm and is insulated from other parts of the vessel by a Teflon ring. Gas is fed into the electrode by a tube (1 mm in diameter, 80 mm in length) running through the vessel lid and subsequently flows into the space below. Here, a hollow cylindrical aluminium cavity is mounted with an internal diameter of 175 mm and a height of 76 mm. Two metal antennas, which serve as a transmitter-receiver pair for low-power microwave (2–8 GHz) signals, pierce the inside of the cavity. The transmitter is connected to a (computer-controlled) microwave generator and the receiver to the data acquisition system. Two centimetre-sized slits, placed opposite to each other in the cavity's circumferential wall and perpendicular to the antennas' plane, enable the laser beam (see below) to pass through the cavity. Gas exits the cavity through its bottom lid containing numerous holes and subsequently flows into the vacuum vessel. Inside the cavity, the gas is assumed to have the same and uniform temperature as controlled by the heating system described above. This is because the cavity is in thermal contact with the heated cavity lid. Moreover, the gas resides sufficiently long in the small tube through which it is transported through the cavity lid to adopt its temperature. A photograph of the cavity is shown in figure 1.

Gas exits the vacuum vessel at the bottom and is then pumped away by, respectively, a turbo-molecular pump and a rotary roughing pump. The pressure inside the vessel is controlled by a regulator valve between the vessel and the pumps within the range of about 5 μPa to 10^5 Pa. However, for normal plasma operation the pressure is in the range 10–15 Pa. Pure argon, oxygen and acetylene flows are controlled by Brooks mass flow controllers (Model 5850E) and are mixed to a single line connected to the gas inlet in the vessel lid. Four quartz windows allow observation of the vessel's interior of which two allow passage of the laser beam through the cavity. A function generator (Agilent 33250A, set to 13.56 MHz), an RF amplifier (Amplifier Research Model 75A250) and a homemade matchbox deliver the power (about 6 W is dissipated by the plasma) capacitively to the plasma. The whole setup is schematically drawn in figure 2.

The LIP experiments are performed using a pulsed frequency-tripled (355 nm) Nd : YAG laser (Continuum
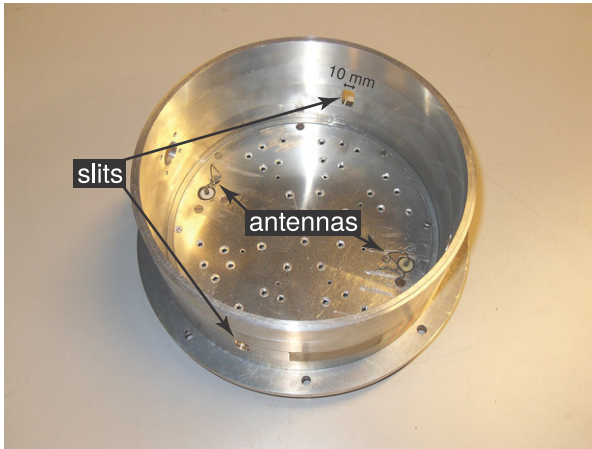
Figure 1. Photograph of the cavity, showing the position of the slits and the microwave antennas.

Figure 2. Schematic of the experimental setup. The laser beam is perpendicular to the paper. The laser itself is not shown.

Powerlite 9030), producing short (3–7 ns) pulses of about 100 mJ per pulse. In figure 2 only the outgoing beam is indicated.

For a detailed description of the triggering of the experiment as well as the data acquisition system the reader is referred to [2].

Two methods, MCRS and LIP, are used. These methods are extensively described in [2, 15–17]. Here a description of the main aspects will suffice.

2.2. Microwave cavity resonance spectroscopy

Using a discharge chamber as a resonance cavity, the electron density of the plasma can be determined using microwaves (since the frequency should be higher than the plasma electron frequency) to excite the resonances. The electron density is determined by comparing the resonance frequency of a cavity devoid of plasma (f_0, signifying the situation of zero electron density) with that of a cavity filled with plasma (frequency f),
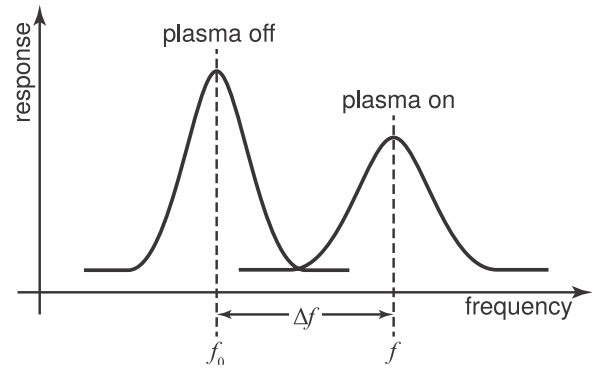
Figure 3. Schematic representation of the cavity response with and without the plasma. Using the two frequencies and frequency difference depicted in the illustration the electron density of the plasma can be determined.

at one resonant mode of the cavity. From the difference of the two frequencies, the electron density follows from

$$\overline{n}_e = \frac{8\pi^2 m_e \epsilon_0 f^2}{e^2} \frac{\Delta f}{f_0},\qquad(6)$$

with m_e and e the electron mass and charge, respectively, ϵ_0 the permittivity of free space and $\Delta f \equiv f - f_0$. See figure 3 for two example cavity responses that illustrate the two frequencies and frequency range. Since the electrons are not homogeneously distributed over the cavity volume, $\overline{n}_e$ means an electric-field-weighted electron density:

$$\overline{n}_e = \frac{\int_{\text{cavity}} n_e(\vec{x}) E^2(\vec{x})\, \mathrm{d}^3\vec{x}}{\int_{\text{cavity}} E^2(\vec{x})\, \mathrm{d}^3\vec{x}},\qquad(7)$$

with $n_e(\vec{x})$ the electron density and $E(\vec{x})$ the electric field magnitude at point $\vec{x} = (x, y, z)$ in space. The integrals are volume integrals evaluated over the total cavity volume.

As a raw data set the cavity response (in volt) is obtained both as a function of time and microwave frequency: $V(t, f)$. This can be visualized as the density plot shown in figure 4. The resonance frequency is obtained by fitting (for all times) the cavity response in frequency space by a trigonometric Fourier series consisting of two harmonics (to account for the asymmetry of the peak). At one moment in time this corresponds to the fitting function

$$V_{\text{fit}}(f) = a_0 + \sum_{n=1}^{2} [a_n \cos(n\omega f) + b_n \sin(n\omega f)],\qquad(8)$$

with a_0, a_n, b_n and ω the fitting parameters. The frequency at which this function is maximum is taken as the resonance frequency. Figure 5 shows a sample fit demonstrating the excellent agreement between measurement data and fit.

The electron density is calculated by taking for f_0 in (6) the resonant frequency during the plasma-off time (up to 0.5 ms in figure 4) and by taking for f the time-dependent value of the resonant frequency.
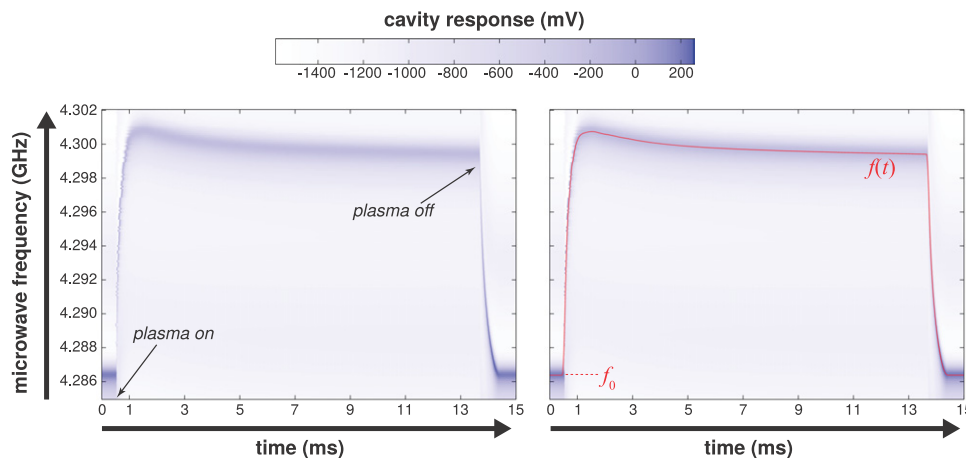
Figure 4. Visualization of the raw data set for an MCRS experiment of an argon–acetylene plasma at 10 Pa and 30 °C. The cavity response is plotted as shades of blue as a function of both time and microwave frequency. The right picture shows the result after fitting in red, corresponding to the temporal evolution of the resonance frequency.
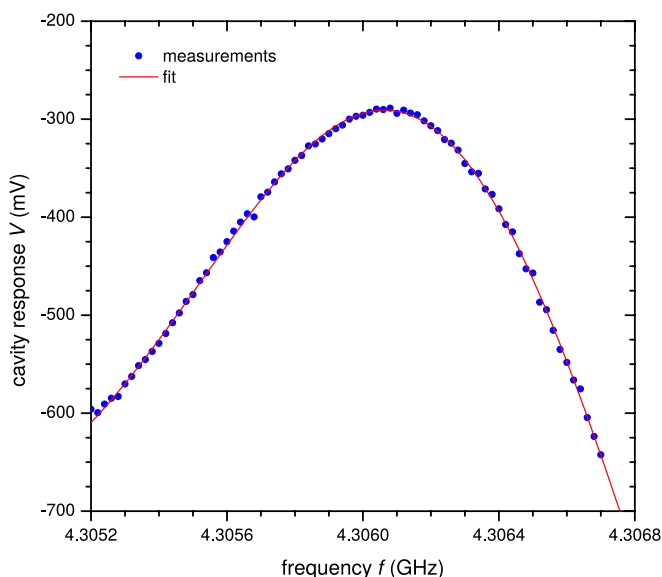
Figure 5. Example cavity response around the TM_{112} resonance (blue dots) fitted with a two-component Fourier (red curve). The frequency at which this function is maximum is taken as the resonance frequency.

In practice, we can only monitor the cavity response at one microwave frequency at a time. So, to obtain a complete data set, the temporal measurements should be performed (repeated) for a range of microwave frequencies. Between measurements at different frequencies the plasma is switched off and back on, with 5 s in between, to allow for any built-up dust and (an)ions to be pumped away. We will also study the plasma at different pressures and temperatures. Between these measurements the vessel is evacuated for at least 120 s. At the start of the whole measurement series the vessel is cleaned by a 300 s pure oxygen plasma to destroy any hydrocarbon residue on the cavity walls.

This method is able to provide electron densities within an uncertainty of less than 0.1%. However, the estimated error in the average electron density is about 10%, since sufficient knowledge about the electron density profile is lacking [15].

Table 1. Threshold energies (i.e. electron affinities) of several photodetachment reactions. Data taken from [18, 19].

| Reaction	Threshold energy (eV)
$H_2CC^- + h\nu \longrightarrow C_2H_2 + e^-$	0.490 ± 0.006
$C_2H^- + h\nu \longrightarrow C_2H\cdot + e^-$	2.956 ± 0.020
$C_4H^- + h\nu \longrightarrow C_4H\cdot + e^-$	3.558 ± 0.015
$C_6H^- + h\nu \longrightarrow C_6H\cdot + e^-$	3.809 ± 0.015
$C_8H^- + h\nu \longrightarrow C_8H\cdot + e^-$	3.966 ± 0.010

2.3. Laser-induced photodetachment

If a laser pulse is shot through a plasma-filled cavity, containing negative ions or charged dust particles, electrons will be detached from negatively charged species (provided their electron affinity is below the laser (photon) energy), through a process called laser-induced photodetachment:

$$X^- + h\nu \longrightarrow X + e^-. \tag{9}$$
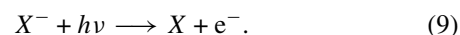
Here, X is an electronegative atom or molecule, $h\nu$ symbolizes the laser photon and e^- an electron. Table 1 summarizes the electron affinities of anions likely to be present in an acetylene (C_2H_2) plasma. Our laser is tuned to a wavelength of 355 nm, corresponding to a photon energy of $h\nu = 3.50$ eV. When the anions in question are in their ground state (see also below), the laser can initiate the upper two reactions only. Other laser-induced reactions that produce free electrons (such as photo-ionization) require much higher energy and do not occur [20]. Note, however, that the electron affinity of the C_4H^- ion is only slightly above (0.058 eV) the laser photon energy. An increase in gas temperature from 30 to 120 °C (0.008 eV) might lead to more vibrationally excited anions. Hence, increasing the gas temperature might enlarge the probability of incident contributions of photodetachment of C_4H^- to the total photodetachment signal. However, we will neglect this possible contribution and assume that a 355 nm laser pulse removes only electrons from C_2H^- and H_2CC^-. This makes any corresponding electron density change directly correlated with the density of these smallest anions, symbolized by n_-.
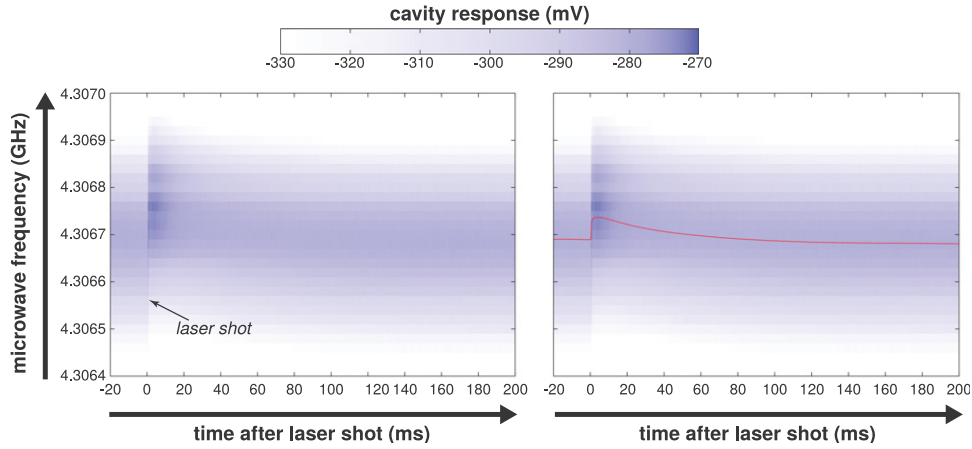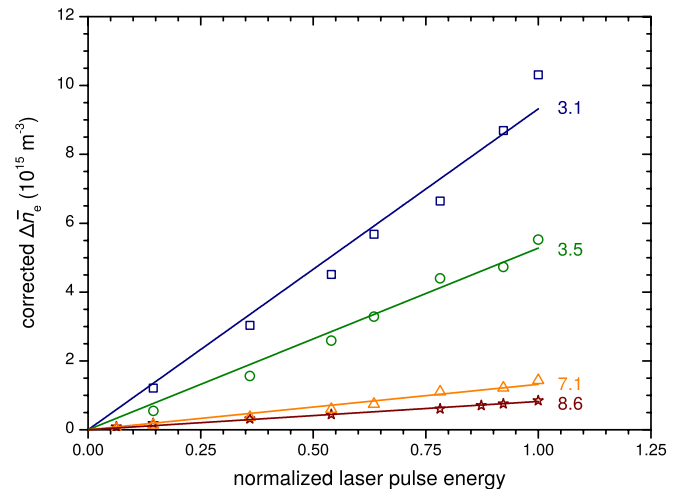
Figure 6. Visualization of the raw data set for one-pulse LIP. The cavity response is plotted as shades of blue as a function of both time and microwave frequency. The effect of the laser pulse is clearly observable. The right picture shows the result after fitting in red, corresponding to the temporal evolution of the resonance frequency. The red curve alone is shown in figure 7.
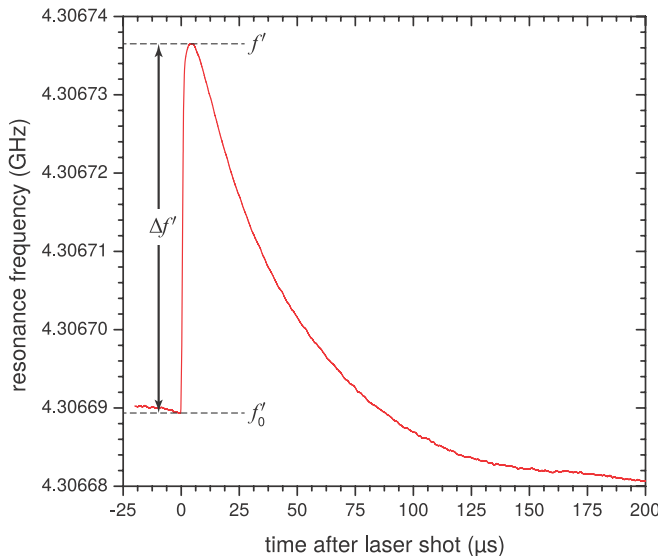
Figure 7. Example of the resonance frequency before and after one-pulse LIP. Using the indicated frequencies and frequency range in (6) the electron density increase $\Delta\bar{n}_e$ due to the laser pulse can be calculated.

Figure 8. Photodetached electron density $\Delta\bar{n}_e$ as a function of (normalized) laser pulse energy. The annotations refer to the laser beam diameter in mm. The plotted values for $\Delta\bar{n}_e$ are corrected for the ratio between the cavity volume and the laser beam volume, $V_{cavity}/V_{laser} = R_{cavity}h_{cavity}/2R_{laser}^2$.

Since a change in electron density also changes the resonance frequency, the effect of the laser pulse is directly observable using MCRS for which a typical raw data set is presented in figure 6. Between measurements at different microwave frequencies, the plasma is switched off (200 μs after the laser shot) and after 5 s back on. If (6) is applied right before and after one-pulse LIP, the calculated electron density is the laser-induced change in electron density, symbolized by $\Delta\bar{n}_e$. Figure 7 shows an example of the resonance frequency of the cavity during one-pulse LIP. The very steep rise during the laser shot corresponds to the actual photodetachment of electrons from C_2H^- and/or H_2CC^-, after which these electrons slowly diffuse and (re-)attach to ions or radicals, decreasing the free electron density and causing the resonance frequency to drop correspondingly.

Generally, the density of the smallest anions that are probed by the laser (C_2H^- and H_2CC^- in our case) is,

at constant laser pulse energy, directly proportional to the photodetached electron density [21], i.e. $n_- \propto \Delta\bar{n}_e$.

However, if the laser pulse energy is increased so, too, does the measured $\Delta\bar{n}_e$. As a function of laser pulse energy E, $\Delta\bar{n}_e$ follows a $1 - \exp(-E)$ behaviour [21]: at low energy being linear and at higher energies levelling off associated with the situation where all anions in the laser path undergo photodetachment. Ideally, one would want to operate in this region of saturation, because then $n_- = \Delta\bar{n}_e$ (provided the laser pulse liberates one electron from an anion), and n_- is determined in absolute terms. If one is bound by a maximum laser pulse energy and no saturation is observed, increasing the laser pulse fluence makes it easier to achieve saturation. Saturation was not readily observed under our initial experimental conditions and photodetachment was also studied at higher fluences. However, in no cases was saturation observed, as shown in figure 8. The laser fluence was increased by collimating the original laser beam diameter of 8.6 mm
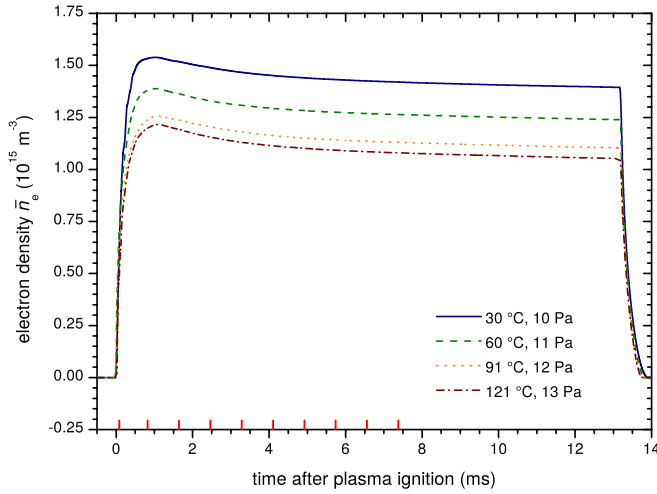
Figure 9. Field-weighted electron density $\bar{n}_e$ in an argon–acetylene plasma as a function of time under four different macro-physical conditions. At around 13 ms the plasma was switched off. The red dashes on the time axis indicate the times at which the laser will be shot during the LIP experiments.

Figure 10. Photodetached electron density ($\Delta\bar{n}_e$) as a function of time after plasma ignition, which is directly proportional to the density of the smallest anions (C_2H^- and H_2CC^-), n_-. The dashed curves serve as a guide to the eye.

by a positive and a negative lens. The figure shows the photodetached electron density $\Delta\bar{n}_e$ multiplied by the cavity to laser beam volume, $V_{cavity}/V_{laser} = R_{cavity}h_{cavity}/2R_{laser}^2$, with R_{cavity} and h_{cavity} the radius and height of the cavity, respectively, and R_{laser} the radius of the laser beam. The horizontal axis shows the energy of the laser pulse normalized to its maximum value of about 100 mJ. Even at the highest fluence no saturation is observed. The results presented in section 3.2 are obtained at a constant full laser power and with a beam diameter of 8.6 mm, for which $n_- \propto \Delta\bar{n}_e$ of course still holds.

3. Results and discussion

3.1. Electron density

For an argon–acetylene plasma (flows: 9.1 sccm argon and 1.9 sccm acetylene), the electron density is determined using MCRS of the TM_{112} resonance with the corresponding resonance frequency $f_0 \approx 4.3$ GHz. This specific resonance was chosen for its high quality factor $Q = 1800$. This yields a cavity response time of $\tau = Q/(\pi f_0) = 134$ ns, being fast enough to follow the processes under investigation. The electron density was determined at four gas temperatures while keeping the neutrals' density constant. The studied pressure–temperature combinations were 10 Pa at 30 °C, 11 Pa at 60 °C, 12 Pa at 91 °C and 13 Pa at 121 °C. About half an hour was given to each gas mixture to equilibrate before taking the measurements. Figure 9 shows the field-weighted electron density for these conditions. The electron density quickly reaches a maximum to only then slowly level off to reach a steady state. Physically, at some point the production of electrons (from, e.g., ionization of argon) cancels out the loss of electrons (through, e.g., DEA onto acetylene). Increasing the gas temperature lowers the maximum as well as the state–state electron density. However, the time at which the maximum is reached is the same for all temperatures: at about
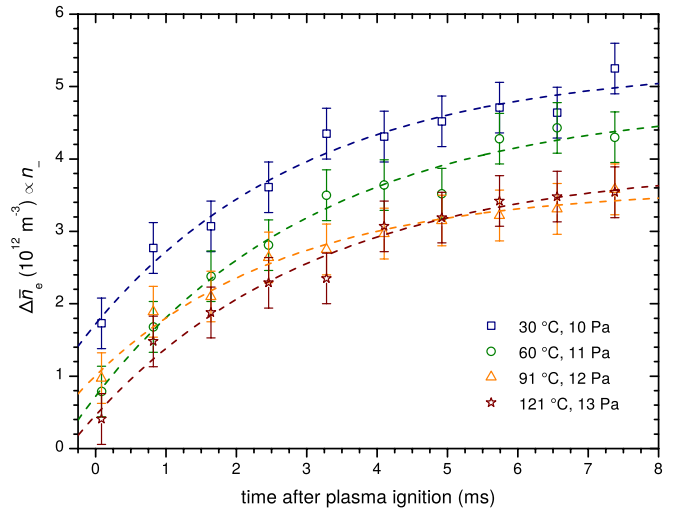
1 ms after plasma ignition. An important consequence of the lower electron density with increasing gas temperature is that, apparently, the balance between production and destruction of anions shifts towards production for higher gas temperatures. If these electrons are lost to C_2H^- and/or H_2CC^- this should be apparent in the anion density measurements (section 3.2) by showing an increased anion density at higher gas temperatures.

3.2. Anion density

LIP experiments were performed by firing the laser through the discharge at different moments after plasma ignition; namely, at $\tau = 0.082, 0.82, 1.64, 2.46, 3.28, 4.10, 4.92, 5.74, 6.56$ and 7.38 ms. These correspond to the red dashes on the time axis in figure 9. Every τ corresponds to a single measurement, as described in section 2.3. Between the measurements at different τ, the vessel is evacuated for at least 120 s. As above, we will also study the plasma at the same four pressure–temperature combinations. The vessel is thoroughly cleaned between each series by evacuating it and by a subsequent oxygen plasma burn of 300 s. The reproducibility of the experiment was checked by performing consecutive LIP measurements under constant plasma conditions over the course of two days, which showed an accuracy of about 10% in $\Delta\bar{n}_e$ values.

Figure 10 shows $\Delta\bar{n}_e$, which is directly proportional to the density of the smallest ions (C_2H^- and H_2CC^-), n_-, for all pressure–temperature combinations. This density shows quite a different temporal behaviour from the electron density. As a function of time it increases and slowly relaxes to a steady state at about 7 ms. Thus, with time, the destruction of C_2H^- and H_2CC^- cancels out production terms more and more. The behaviour as a function of temperature is more or less similar to that found for the overall electron density; increasing the temperature generally limits the measured anion density and saturates at about 90 °C. This is, however, not what we expected from the electron density measurements (figure 9) and this will be interpreted in the next section.
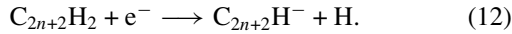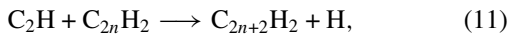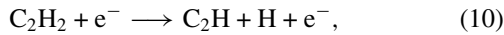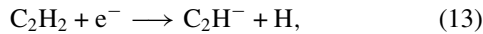
3.3. Physical interpretation

We observe that increasing the gas temperature (T_g) lowers both the electron density and the density of the smallest anions (C_2H^- and H_2CC^-), n_-. From the downwards trend of $\overline{n}_e$ with increasing T_g, we concluded that by increasing T_g the anion production rate also increases. The only reasonable explanation for the fact that n_- shows the opposite behaviour with T_g is that larger anions, such as C_4H^- and C_6H^-, are produced at a faster rate than C_2H^- and H_2CC^-. In other words, the total production of all anionic species together is indirectly reflected in the behaviour of $\overline{n}_e$, whereas with LIP at 355 nm only the smallest anions (C_2H^- and H_2CC^-) are sampled.

Other possible loss processes of the smallest anions are autodetachment and recombination with positive ions in our discharge. Autodetachment is highly unlikely to occur as both species are very stable with respect to this process [9, 10] and the relative reaction rate for recombination of C_2H^-/H_2CC^- with respect to that of the higher anions is not gas temperature dependent [9]. So, these loss channels cannot explain the observed results.
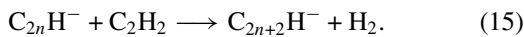
We now look at the chemistry behind the formation of the larger anions, which can be initiated either by neutrals (radicals) or anions. The first reaction pathway is ($n = 1, 2, 3, \ldots$)

$$C_2H_2 + e^- \longrightarrow C_2H + H + e^-, \tag{10}$$

$$C_2H + C_{2n}H_2 \longrightarrow C_{2n+2}H_2 + H, \tag{11}$$

$$C_{2n+2}H_2 + e^- \longrightarrow C_{2n+2}H^- + H. \tag{12}$$

The second reaction pathway is for C_2H^- ($n = 2, 3, 4, \ldots$):

$$C_2H_2 + e^- \longrightarrow C_2H^- + H, \tag{13}$$

$$C_2H^- + C_2H_2 \longrightarrow C_4H^- + H_2, \tag{14}$$

$$\vdots$$

$$C_{2n}H^- + C_2H_2 \longrightarrow C_{2n+2}H^- + H_2. \tag{15}$$

For H_2CC^- it is

$$C_2H_2 + e^- \longrightarrow H_2CC^-, \tag{16}$$

$$H_2CC^- + C_2H_2 \longrightarrow C_4H_2^- + H_2, \tag{17}$$
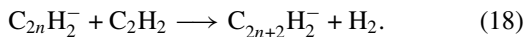
$$\vdots$$

$$C_{2n}H_2^- + C_2H_2 \longrightarrow C_{2n+2}H_2^- + H_2. \tag{18}$$

These last two reaction pathways can also occur with larger neutral polymers ($C_{2n+2}H_2$; $n = 1, 2, 3, \ldots$) as a precursor. However, since acetylene is the feed gas it is the dominant precursor neutral.

During ion–neutral polymerization reactions, the ions induce a dipole moment in the neutral molecule. Therefore, ion–neutral reactions typically are ten times faster than reactions between neutral molecules [22]. From this we conclude that the faster latter pathways (reactions (13)–(15)

and (16)–(18)) dominate in the production of the larger anions. In other words, the production of all negative ions (at least on these short timescales) is dominated by polymerization chain reactions starting from the smallest anions, C_2H^- and H_2CC^-; a conclusion which is supported by mass spectrometric measurements of Deschenaux *et al* [6]. The measurements of $\overline{n}_e$ clearly show a total anion density increase with higher T_g, which means that the production rate of C_2H^- and H_2CC^- should also be enhanced. This does, however, not show in the measurements of n_-, meaning that their destruction rate increases even more so with T_g. C_2H^- and H_2CC^- are produced by DEA onto acetylene (reactions (13) and (16)) and are destructed by polymerization with acetylene (reactions (14) and (17)). No temperature dependences of the rate constant for DEA onto acetylene are found in the literature. For the ion–neutral polymerization reactions with acetylene, the literature reports independence of T_g [22]. This must lead to the conclusion that another polymerization reaction is responsible for the destruction of C_2H^- and/or H_2CC^- and it becomes more important at higher T_g. A probable candidate is polymerization of C_2H^- and/or H_2CC^- with (vibrationally) excited acetylene, which is present at higher concentrations at higher T_g. Thus, with higher T_g, C_2H^- and/or H_2CC^- tend(s) to react with excited acetylene molecules rather than with ground-state molecules.

4. Conclusions

Absolute (field-weighted) electron densities as a function of time were accurately determined in argon–acetylene radio-frequency plasmas by means of microwave cavity resonance spectroscopy (MCRS) of the TM_{112} resonance of our cavity. The electron density shows a maximum at about 1 ms after plasma ignition, only then to level off to reach a steady-state value. This is explained by the formation of negative ions such as C_2H^- and H_2CC^- by dissociative electron attachment onto acetylene. While keeping the neutrals' density constant, increasing the gas temperature limits the number of free electrons, which suggests a density increase of all anions together with elevated gas temperatures.

The density of the smallest anions (C_2H^- and H_2CC^-) was determined by combining MCRS with laser-induced photodetachment using a powerful laser tuned to 355 nm. It was found that the density of the smallest anions steadily increases in the first few milliseconds after plasma ignition, after which it reaches a steady state. While keeping the neutrals' density constant, increasing the gas temperature decreases the density of the smallest anions, saturating at a temperature of about 90 °C. The found gas-temperature dependence of the ion–neutral polymerization reactions is explained by an increasing number of (vibrationally) excited precursor molecules present at elevated temperatures.

References

[1] Stoffels W W, Stoffels E, Kroesen G M W and de Hoog F J 1995 Electron density fluctuations in a dusty Ar/SiH$_4$ rf discharge *J. Appl. Phys.* **78** 4867–72

[2] Sorokin M 2005 Dust particle formation in silane plasmas *PhD Thesis* Eindhoven University of Technology

[3] Boufendi L, Jouanny M Ch, Kovacevic E, Berndt J and Mikikian M 2011 Dusty plasma for nanotechnology *J. Phys. D: Appl. Phys.* **44** 174035

[4] Beckers J, Stoffels W W and Kroesen G M W 2009 Temperature dependence of nucleation and growth of nanoparticles in low pressure Ar/CH$_4$ RF discharges *J. Phys. D: Appl. Phys.* **42** 155206

[5] Buss R J and Hareland W A 1994 Gas phase particulate formation in radiofrequency fluorocarbon plasmas *Plasma Sources Sci. Technol.* **3** 268

[6] Deschenaux Ch, Affolter A, Magni D, Hollenstein Ch and Fayet P 1999 Investigations of CH$_4$, C$_2$H$_2$ and C$_2$H$_4$ dusty RF plasmas by means of FTIR absorption spectroscopy and mass spectrometry *J. Phys. D: Appl. Phys.* **32** 1876

[7] Benedikt J, Consoli A, Schulze M and von Keudell A 2007 Time-resolved molecular beam mass spectrometry of the initial stage of particle formation in an Ar/He/C$_2$H$_2$ plasma *J. Phys. Chem.* A **111** 10453–9

[8] Stoykov S, Eggs C and Kortshagen U 2001 Plasma chemistry and growth of nanosized particles in a C$_2$H$_2$ RF discharge *J. Phys. D: Appl. Phys.* **34** 2160

[9] De Bleecker K, Bogaerts A and Goedheer W 2006 Detailed modeling of hydrocarbon nanoparticle nucleation in acetylene discharges *Phys. Rev.* E **73** 026405

[10] Mao M, Benedikt J, Consoli A and Bogaerts A 2008 New pathways for nanoparticle formation in acetylene dusty plasmas: a modelling investigation and comparison with experiments *J. Phys. D: Appl. Phys.* **41** 225201

[11] Wörner L, Kovacevic E, Berndt J, Thomas H M, Thoma M H, Boufendi L and Morfill G E 2012 The formation and transport phenomena of nanometre-sized particles in a dc plasma *New J. Phys.* **14** 023024

[12] Mitic S, Pustylnik M Y, Morfill G E and Kovačević E 2011 In situ characterization of nanoparticles during growth by means of white light scattering *Opt. Lett.* **36** 3699–701

[13] Berndt J, Kovačević E, Stefanović I and Boufendi L 2009 Controlled dust formation in pulsed rf plasmas *J. Appl. Phys.* **106** 063309

[14] Bouchoule A (ed) 1999 *Dusty Plasmas: Physics, Chemistry and Technological Impacts in Plasma Processing* (New York: Wiley)

[15] Stoffels-Adamowicz E and Stoffels W W 1994 Electrons, ions and dust in a radio-frequency discharge *PhD Thesis* Eindhoven University of Technology

[16] Stoffels E, Stoffels W W, Vender D, Kando M, Kroesen G M W and de Hoog F J 1995 Negative ions in a radio-frequency oxygen plasma *Phys. Rev.* E **51** 2425–35

[17] Haverlag M 1991 Plasma chemistry of fluorocarbon RF discharges used for dry etching *PhD Thesis* Eindhoven University of Technology

[18] Taylor T R, Xu C and Neumark D M 1998 Photoelectron spectra of the C$_{2n}$H$^-$ ($n = 1 - 4$) and C$_{2n}$D$^-$ ($n = 1$–3) anions *J. Chem. Phys.* **108** 10018–26

[19] Haynes W M (ed) 2011–2012 Electron Affinities (table) *CRC Handbook of Chemistry and Physics* 92nd edn (Boca Raton, FL: CRC Press/Taylor and Francis) (Internet Version)

[20] Haynes W M (ed) 2011–2012 Ionization energies of gas-phase molecules (table) *CRC Handbook of Chemistry and Physics* 92nd edn (Boca Raton, FL: CRC Press/Taylor and Francis) (Internet Version)

[21] Bacal M, Hamilton G W, Bruneteau A M, Doucet H J and Taillet J 1979 Measurement of H$^-$ density in plasma by photodetachment *Rev. Sci. Instrum.* **50** 719–21

[22] Benedikt J 2010 Plasma-chemical reactions: low pressure acetylene plasmas *J. Phys. D: Appl. Phys.* **43** 043001